PHYSICS OF FLUIDS **17**, 075102 (2005)

Pressure drop and heat transfer rates in forced convection rotating square duct flows at high rotation rates

J. Pallares and F. X. Grau
Department of Mechanical Engineering, University Rovira i Virgili, Av. Països Catalans 26, 43007 Tarragona, Spain

L. Davidson
Department of Thermo and Fluid Dynamics, Chalmers University of Technology, SE-412 96 Gothenburg, Sweden

(Received 13 May 2004; accepted 28 April 2005; published online 21 June 2005)

This paper presents and discusses numerical simulations of forced convection heat transfer in a rotating square duct at high rotation rates. The mean pressure gradient has been kept constant in the simulations that were conducted with a second order finite volume code with a dynamical localized subgrid scale model. The rotation number based on the bulk velocity ($\mathrm{Ro}=2\Omega D/\overline{U_b}$) was varied from 0.12 to 6.6 and consequently the Reynolds number ($\mathrm{Re}=\overline{U_b}D/\nu$) ranged from 3900 to 1810 according to the fact that rotation tends to increase the pressure drop in the duct. A model for estimating the velocities and the corresponding friction coefficient has been developed by analytically solving simplified versions of the momentum budgets within the Ekman layers occurring near the opposite two walls of the duct perpendicular to the rotation axis. The model reproduces accurately the velocity profiles of the numerical simulation at high rotation rates and predicts that the boundary layer quantities scale as $Ek^{1/2}$ ($Ek=\nu/\Omega D^2$). At $\mathrm{Ro}>1$ the Ekman layers are responsible for most of the pressure drop of the flow while the maximum heat transfer rates are found on the wall where the stratification of the x-momentum is unstable with respect to the Coriolis force. Rotation enhances the differences between the contributions of the local friction coefficients and local Nusselt numbers of the four walls of the duct and considerably increases, in comparison with the non-rotating case, the pressure drop of the flow and the Nusselt number. The overall friction coefficient of the measurements and the simulations existing in the literature, as well as the present numerical predictions, are well correlated with the equation $1.09(\mathrm{Cf}/Ek^{1/2})^{1.25}=\mathrm{Ro}$ in the range $\mathrm{Ro}\geqslant 1$ for $\mathrm{Re}\leqslant 10^4$. © *2005 American Institute of Physics*. [DOI: 10.1063/1.1941365]

I. INTRODUCTION

The prediction and the analysis of the effects of rotation on duct flows have been motivated mainly by their implications in engineering fields concerned with flow and heat and mass transfer processes in rotating devices that can be encountered in technologies such as turbine blade cooling, conventional centrifugal separation and centrifugal membrane separation. Numerical and experimental studies dealing with turbulent channel flows, subjected to rotation around an axis parallel to the spanwise direction, have shown that the turbulent mixing of fluid particles is enhanced in the regions of the flow where the streamwise momentum is unstably stratified with respect to the Coriolis force (unstable side or pressure side) while a reduction of mixing is observed where the streamwise momentum is stably stratified (stable side or suction side).[1–3]

In finite aspect ratio ducts, the Coriolis force generates persistent secondary flows that contribute to the mixing processes between the stable and unstable side of the duct. Essentially, the time averaged secondary flows consist in two large counter-rotating cells that convect low momentum fluid from the stable side to the unstable side across the central region of the duct and from the unstable to the stable side along the sidewalls.[4,5] The convective transport in the central region of the duct displaces the maximum of the streamwise velocity component toward the unstable wall and consequently reduces the extension of the cross section of the duct in which the unstable stratification occurs. At sufficient large rotation rates the flow in the stable side can be relaminarized. In spite of the corresponding augmentation of the mean shear rate in the unstable side, as the rotation rate is increased, there is an overall reduction of the turbulent kinetic energy produced by the convective transport from the stable side to the unstable side of the secondary flows.

The head loss and the overall heat transfer rate are considerably increased by the effect of rotation in comparison with the non-rotating case, as reported in numerical simulations[4] and experiments.[6] At the Reynolds number considered in these works ($\mathrm{Re}\approx 10^4$) the increase of the overall friction coefficients and Nusselt number is produced by the augmentation of the mean shear rate in the unstable side and by development of the Ekman layers along the walls of the duct perpendicular to the rotation axis.

This study analyzes the effect of rotation on the friction coefficient and Nusselt numbers at low Reynolds numbers ($\mathrm{Re}<3900$). The physical and mathematical models are described in Sec. II and the numerical results are presented and discussed in Sec. III.

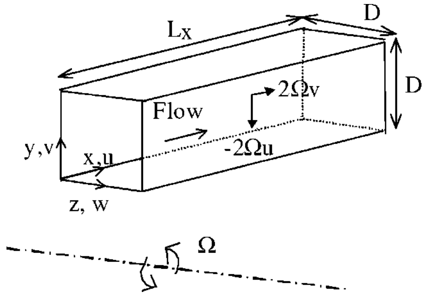

FIG. 1. Physical model and coordinate system.

II. MODEL

Figure 1 shows the physical model and the coordinate system adopted. The duct is rotating with a constant rotation rate with respect to an axis parallel to the z direction, $\vec{\Omega} = (0,0,\Omega)$, as indicated in Fig. 1. The four walls of the duct are heated with a uniform and constant axial wall heat flux (q''_w) and constant peripheral wall temperature. This boundary condition denoted as H1, following the nomenclature proposed by Shah and London,[7] idealize practical situations in which the axial heat rate per duct length is constant and the wall conductance, defined as the ratio between the wall (k_w) and the fluid (k) thermal conductivities multiplied by the ratio between the hydraulic diameter of the duct (D) and the wall thickness (d) (i.e., $C=k_w D/k\, d$), attains large values. The flow, which is driven by an externally imposed pressure gradient, is assumed to be hydrodynamically and thermally fully developed. The physical properties of the fluid, with a Prandtl number of 0.7, are assumed to be constant and the gravitational and centrifugal buoyancy effects are neglected.

The large-eddy simulation (LES) technique has been used to keep the computational requirements at a moderate level for the turbulent flow simulations. The resolved scales and the corresponding governing transport equations are defined by the filtering operation. The non-dimensional filtered continuity, momentum and thermal energy equations are

$$\frac{\partial u_i}{\partial x_i} = 0, \tag{1}$$

$$\frac{\partial u_i}{\partial t} + \frac{\partial u_j u_i}{\partial x_j} = 4\delta_{1j} - \frac{\partial p}{\partial x_i} - \frac{\partial \tau_{ij}}{\partial x_j} + \frac{1}{\mathrm{Re}_\tau}\frac{\partial^2 u_i}{\partial x_j \partial x_j} + \epsilon_{ij3}\mathrm{Ro}_\tau u_j, \tag{2}$$

and

$$\frac{\partial \theta}{\partial t} + \frac{\partial u_j \theta}{\partial x_j} = 4\delta_{1j}\frac{u_j}{U_b} - \frac{\partial h_j}{\partial x_j} + \frac{1}{\mathrm{Pr}\,\mathrm{Re}_\tau}\frac{\partial^2 \theta}{\partial x_j \partial x_j}, \tag{3}$$

respectively.

The scales used to obtain the non-dimensional variables are the hydraulic diameter of the duct (D), the average friction velocity (u_τ) and the friction temperature $(T_\tau = q''_w/\rho C p u_\tau)$. The non-dimensional temperature is defined as $\theta = (\langle T_w\rangle - T)/T_\tau$, where $\langle T_w\rangle$ is the peripheral wall temperature that is independent of y and z and varies linearly along the x direction according to the fully developed assumption. Under this condition the variation of the bulk temperature and the peripheral wall temperature along the streamwise direction can be written as $dT_b/dx = d\langle T_w\rangle/dx = 4q''_w/\rho C p \overline{U}_b D$. Pressure is scaled with the average wall shear stress, $\tau_w = \rho u_\tau^2$.

The different terms on the right-hand side of Eq. (2) are, from left to right, the imposed non-dimensional pressure gradient along the streamwise direction, the gradient of the fluctuating pressure, the subgrid scale contribution, the viscous diffusion term and the Coriolis term. Figure 1 shows the direction of the components of the Coriolis acceleration according to the system of coordinates adopted. The centrifugal acceleration, which is considered constant, is included in the non-dimensional mean pressure gradient. In Eq. (2), ϵ is the Levi–Civita's alternating tensor and $\mathrm{Re}_\tau = u_\tau D/\nu$ and $\mathrm{Ro}_\tau = 2\Omega D/u_\tau$ are the Reynolds and the rotational numbers, respectively. The first term on the right-hand side of the thermal energy balance [Eq. (3)] corresponds to the non-dimensional mean temperature gradient along the streamwise direction. In this term, U_b is the non-dimensional bulk velocity $(U_b = \overline{U}_b/u_\tau)$. The second and third terms on the right-hand side of Eq. (3) are responsible for the subgrid scale transport and the heat conduction, respectively.

The Reynolds number based on the hydraulic diameter of the duct and the averaged friction velocity has been kept constant in the simulations, $\mathrm{Re}_\tau = 300$ (i.e., constant imposed pressure gradient) as indicated in Table I that summarizes the complete set of simulations analyzed in this study. The rotation numbers were increased from $\mathrm{Ro}_\tau = 3$ to $\mathrm{Ro}_\tau = 40$ and, consequently, the Reynolds number decreased from 3420 to 1810. The numerical simulations were carried out with the CALC-LES code, a finite volume second order accuracy code, using the localized one-equation dynamic subgrid-scale (SGS) model proposed by Kim and Menon.[8] The details about the code and the SGS model can be found in Sohankar *et al.*[9] and Kim and Menon,[8] respectively. This model has been used successfully in the simulations of turbulent rotating channel and duct flows.[5] The localized dynamic SGS model used predicts a negligibly small SGS viscosity ratio (ν_{SGS}/ν) in the regions where the flow has been relaminarized by the effect of rotation or at the lowest Reynolds number considered (Re = 1810). At this low Reynolds number the maximum value of the ratio ν_{SGS}/ν is 10^{-4} and there are no significant differences between the averaged flow fields, local Nusselt numbers and local friction coefficients predicted by LES and direct numerical simulation (DNS). Following Pallares and Davidson,[10] a constant SGS Prandtl number $(\mathrm{Pr}_{\mathrm{SGS}} = \nu_{\mathrm{SGS}}/\alpha_{\mathrm{SGS}} = 0.4)$ was used to compute the SGS heat fluxes according to the small effect of this approximation considering the grid resolution used. These authors did not observe any significant difference between the averaged velocities and temperature distributions, as well as the turbulence intensities and turbulent heat fluxes in simulations of rotating forced convection at low Reynolds numbers and $\mathrm{Ro}_\tau = 1.5$ using two different values of $\mathrm{Pr}_{\mathrm{SGS}}$ $(\mathrm{Pr}_{\mathrm{SGS}} = 0.4$ and $0.8)$. As an example, at $\mathrm{Ro}_\tau = 1.5$, the maximum differences in the averaged temperature profiles near the unstable wall are within 1.5% and the difference of the Nusselt number of both simulations is only 1%. The increase

TABLE I. Non-dimensional numbers of the simulations obtained with a computational domain of dimensions $L_x=6D$, $L_y=L_z=D$ and $66\times66\times66$ grid nodes. (*) Data corresponding to the extended domain ($L_x=12D$, $L_y=L_z=D$ and $130\times66\times66$ grid nodes) and (**) to simulations using a finer grid ($L_x=12D$, $L_y=L_z=D$ and $171\times86\times86$ grid nodes).

Re_τ $(u_\tau D/\nu)$	Ro_τ $(2\Omega D/u_\tau)$	$\mathrm{Re}=\mathrm{U_b}\ \mathrm{Re}_\tau$ $(\overline{U}_b D/\nu)$	$\mathrm{Ro}=\mathrm{Ro}_\tau/\mathrm{U_b}$ $(2\Omega D/\overline{U}_b)$	Cf $(2\tau_w/\rho \overline{U}_b^2)$	Nu (hD/k)	$\mathrm{Ek}^{1/2}$ $(\sqrt{\nu/\Omega D^2})$
300	1.5	3900 $(3880)^*$ $(3860)^{**}$	0.12 $(0.12)^*$ $(0.12)^{**}$	0.01185 $(0.01196)^*$ $(0.01211)^{**}$	16.61 $(16.74)^*$ $(16.80)^{**}$	0.067
	3	3420	0.26	0.01535	18.86	0.047
	5	3080	0.49	0.01885	20.58	0.037
	7	2870	0.73	0.02187	21.82	0.031
	10	2650	1.13	0.02564	22.61	0.026
	20	2250	2.66	0.03548	20.40	0.018
	30	2000	4.49	0.04487	16.39	0.015
	40	1810 $(1810)^*$ $(1820)^{**}$	6.62 $(6.62)^*$ $(6.58)^{**}$	0.05474 $(0.05474)^*$ $(0.05434)^{**}$	13.29 $(13.29)^*$ $(13.33)^{**}$	0.013

of the value of $\mathrm{Pr_{SGS}}$ from 0.4 to 0.8 produces a slight reduction of the SGS thermal diffusivity according to the procedure used to compute the SGS thermal diffusivity ($\alpha_{\mathrm{SGS}}=\nu_{\mathrm{SGS}}/\mathrm{Pr_{SGS}}$). This reduction of the SGS terms in the thermal energy equation is mainly balanced by the increase of the resolved turbulent heat fluxes. It is expected that, as the rotation number is increased, the assumption of a constant value of $\mathrm{Pr_{SGS}}$ becomes even less important because of the overall reduction of the turbulence level of the flow and, consequently, of the contribution of the SGS terms. Under the conditions of the simulations the adoption of a constant $\mathrm{Pr_{SGS}}$ is justified considering that the use of a dynamical procedure to compute the SGS thermal diffusivity doubles the computational cost of the SGS model.

It should be noted that the centrifugal buoyancy effects are not considered in the simulations. The set of non-dimensional parameters ($\mathrm{Re}_\tau=300, 1.5\leqslant\mathrm{Ro}_\tau\leqslant40, \mathrm{Pr}=0.71$) that has been chosen may correspond to physical situations in which air, at ambient temperature and pressure, flows ($U_b\approx6$ m/s) in small ducts ($D\approx5$ mm) in the range of rotation speeds from 1500 rpm to 35 000 rpm, usually encountered in gas turbines and industrial centrifuges. Under these conditions and at $\mathrm{Ro}_\tau\leqslant20$, a wall heat flux density of about 200 W/m^2 produces values of the centrifugal buoyancy parameter,[10] ($\mathrm{Gr}/\mathrm{Re}_\tau^2$), which contributes to the streamwise momentum equation, that are less than 2% of the imposed non-dimensional pressure gradient along the streamwise direction. At higher rotation rates ($30\leqslant\mathrm{Ro}_\tau\leqslant40$) this contribution of the centrifugal buoyancy term is increased up to 35% and the heat transfer results in this range of rotational numbers presented in this study have to be considered with this limitation.

The non-slip boundary condition and a constant non-dimensional temperature ($\theta=0$) were applied at the four walls. Periodic boundary conditions for the non-dimensional velocities, pressure and temperature were used at the inlet and outlet of the duct. The computational domain ($L_x=6D, L_y=L_z=D$) was divided into $66\times66\times66$ grid nodes that were stretched near the wall using a tanh function and uniformly distributed along the homogeneous streamwise direction ($\Delta x^+\approx29$). The minimum and maximum grid spacing in wall coordinates along the directions perpendicular to the walls are $(\Delta y^+)_{\min}=(\Delta z^+)_{\min}\approx0.4$ and $(\Delta y^+)_{\max}=(\Delta z^+)_{\max}\approx9$. The simulations of non-rotating duct flow at $\mathrm{Re}=4500$ using this grid resolution and the dynamic localized SGS model were initially carried out and results were compared successfully in Pallares and Davidson[11] with existing experimental and DNS data.

To determine the effect of the streamwise length of the computational domain and the effect of the grid resolution on the relevant parameters of the rotating duct flow simulations presented in this study, two sets of large-eddy simulations at the minimum and maximum rotational numbers considered ($\mathrm{Ro}_\tau=1.5$ and $\mathrm{Ro}_\tau=40$) have been carried out. In the first set the computational domain has been extended to $L_x=12D, L_y=L_z=D$ using the same grid resolution (i.e., $130\times66\times66$ grid nodes). In the second set the simulations were performed in the extended domain ($L_x=12D, L_y=L_z=D$) increasing the number of grid nodes in each direction 30%. The corresponding grid has $171\times86\times86$ grid nodes and grid spacing of $\Delta x^+\approx22$, $(\Delta y^+)_{\min}=(\Delta z^+)_{\min}\approx0.3$ and $(\Delta y^+)_{\max}=(\Delta z^+)_{\max}\approx7$. Table I shows that the differences between the averaged quantities obtained with the different grid resolutions are within 2% at $\mathrm{Ro}_\tau=1.5$ and only 0.5% at $\mathrm{Ro}_\tau=40$.

III. RESULTS AND DISCUSSION

A. Mean flow and thermal fields

During the simulations, the averaging procedure was started when the flow was statistically fully developed. The flow quantities were averaged along the homogeneous x-direction as well as in time, typically during 50–70 non-dimensional time units. Time and x-direction averaged flow fields progressively tended to be symmetric with respect to $z=0.5$ as the sampling size was increased. Consequently, symmetry of the mean flow field with respect to $z=0.5$ was enforced in order to increase the sampling size.

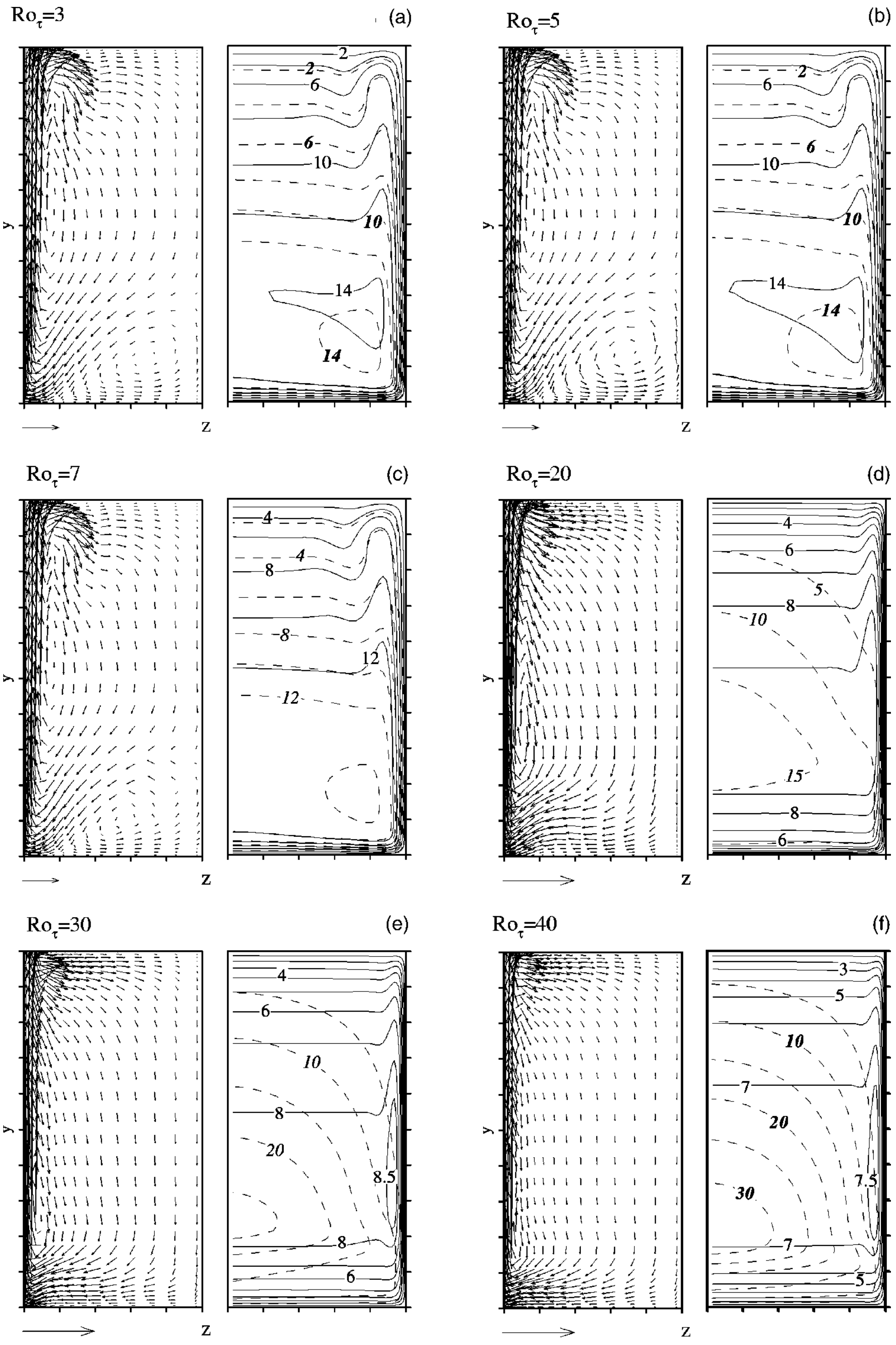

FIG. 2. Averaged flow and temperature contours at (a) $\mathrm{Ro}_\tau=3$, (b) $\mathrm{Ro}_\tau=5$, (c) $\mathrm{Ro}_\tau=7$, (d) $\mathrm{Ro}_\tau=20$, (e) $\mathrm{Ro}_\tau=30$, and (f) $\mathrm{Ro}_\tau=40$. The streamwise velocity/temperature contours are depicted with continuous/dashed lines. The vector near the bottom left corner has a unit length.

Figures 2(a)–2(f) show the average flow fields at $\mathrm{Ro}_\tau=3$, 5, 7, 20, 30, and 40. In these figures, the cross-stream vector fields are represented on the left while the streamwise velocity and temperature contours are depicted on the right. In the left part of Figs. 2(a)–2(f) only every second vector is shown.

The effects of low rotation rates $(0 \leqslant \mathrm{Ro}_\tau \leqslant 1.5)$ in turbulent duct flow at $\mathrm{Re}_\tau=300$ were investigated by Pallares and Davidson.[5] These authors found that at $\mathrm{Ro}_\tau=1.5$ $(\mathrm{Re}=3900)$, the turbulence intensities of the flow are concentrated near the unstable wall $(y=0)$ and near the sidewalls $(z=0$ and $z=1)$. The flow can be considered laminar in the central part of the duct where cross-stream convection of x-momentum from the stable side to the unstable side produces the stabilization of the flow to a Taylor–Proudman regime (i.e., the streamwise velocity component does not vary along the direction of the axis of rotation).

The topologies of the average flow field at $\mathrm{Ro}_\tau \leqslant 7$, shown in Figs. 2(a)–2(c), are similar to that reported in Pallares and Davidson[5] at $\mathrm{Ro}_\tau=1.5$. The averaged cross-stream vector field consists of two large stretched secondary flows near the sidewalls $(z=0$ and $z=1)$ and two small secondary cells near the unstable wall $(y=0)$. The increase of the rotation number from $\mathrm{Ro}_\tau=1.5$ $(\mathrm{Re}=3900)$ to $\mathrm{Ro}_\tau=3$ (Re

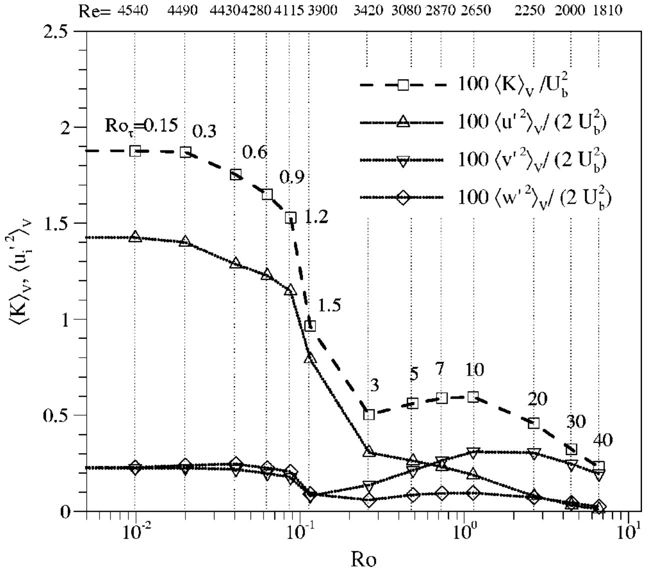

FIG. 3. Volume averaged kinetic energy of the fluctuations and fluctuation intensities at different rotation rates. The corresponding Reynolds numbers ($Re = Re_\tau\ U_b$) are included at the top of the figure. Data of Pallares and Davidson (Ref. 5) in the range $Ro_\tau \leq 1.5$ are also included in this figure.

$=3420$) produces the enlargement of the small secondary cells and a displacement of maxima of the streamwise velocity component toward the sidewalls [see Fig. 2(a)]. These changes in the mean flow field near the unstable wall can be attributed to the reduction of the turbulence intensities in this region. It can be seen in Figs. 2(a)–2(c) that at $Ro_\tau \leq 7$ the distribution of the averaged temperature contours in the cross section of the duct is similar to that of the streamwise velocity component. There is a stratification of the contours of temperature and x-velocity component in the central part of the duct and the corresponding maxima occur near the bottom corners. At $Ro_\tau \geq 20$ the temperature contours have a marked different distribution in comparison with the contours of the streamwise velocity component as shown in Figs. 2(d)–2(f). It can be seen that the temperature distributions are not stratified but have a maximum near the unstable wall in the symmetry plane $z=0.5$. These differences between the x-velocity component and temperature distributions can be attributed to the fact that at high rotation rates the relaminarization of the flow and the important contribution of the Coriolis term in the x-momentum equation completely invalidate the analogy between the x-momentum and the thermal energy balances.

Figure 3 shows the evolution of the non-dimensional volume averaged kinetic energy of the velocity fluctuations, scaled with the bulk velocity, $\langle K\rangle_V = (\langle u'^2\rangle + \langle v'^2\rangle + \langle w'^2\rangle)/2U_b^2$, as a function of the rotational number. The data at $Ro_\tau \leq 1.5$ reported by Pallares and Davidson[5] are also included in this figure. Note that the increase of the rotational number produces a reduction of the Reynolds number ($Re = Re_\tau U_b$) based on the bulk velocity (see Table I), if the averaged pressure gradient along the x-direction, or the value of Re_τ, is kept constant. The scaling chosen for $\langle K\rangle_V$ makes the results at different Reynolds numbers more comparable. As shown in Fig. 3 the important reduction of $\langle K\rangle_V$ in the range $1.2 \leq Ro_\tau \leq 3$ ($4115 > Re > 3420$) corresponds to the decrease of the streamwise Reynolds stress component, $\langle u'^2\rangle$, which receives energy from the production terms that include the main strains ($\partial u/\partial y$ and $\partial u/\partial z$). For example, the reduction of $\langle K\rangle_V$ at $Ro_\tau=1.5$ ($Re=3900$) is 48% and at $Ro_\tau=3$ ($Re=3420$) is 73%, with respect to the volume averaged turbulent kinetic energy of the non-rotating case ($Re=4500$). Figure 3 shows that, in the range $7 \leq Ro_\tau \leq 40$, the fluctuation intensity of the vertical component of the velocity, $\langle v'^2\rangle$, is the main contributor to the unsteadiness of the flow. In this range of rotational numbers the flow in most of the cross section of the duct is laminar and steady and the velocity intensities are confined to the regions near the unstable wall and near the sidewalls. It can be seen in Fig. 3 that the increase of the volume averaged value of $\langle v'^2\rangle$ in the range $3 \leq Ro_\tau \leq 10$ agrees with the maintenance of large secondary cells near the unstable wall [see Figs. 2(a)–2(c)], while the decrease observed in the range $20 \leq Ro_\tau \leq 40$ is related with their disappearance.

B. Averaged momentum and thermal energy budgets

The non-dimensional averaged x- and y-momentum and thermal energy balances can be written as

$$-\left(V\frac{\partial U}{\partial y} + W\frac{\partial U}{\partial z}\right) + \frac{1}{Re_\tau}\left(\frac{\partial^2 U}{\partial y^2} + \frac{\partial^2 U}{\partial z^2}\right) - \left(\frac{\partial\langle u'v'\rangle}{\partial y} + \frac{\partial\langle u'w'\rangle}{\partial z}\right) + SGS_U + Ro_\tau V = -4, \quad (4)$$

$$-\left(V\frac{\partial V}{\partial y} + W\frac{\partial V}{\partial z}\right) + \frac{1}{Re_\tau}\left(\frac{\partial^2 V}{\partial y^2} + \frac{\partial^2 V}{\partial z^2}\right) - \left(\frac{\partial\langle v'^2\rangle}{\partial y} + \frac{\partial\langle v'w'\rangle}{\partial z}\right) + SGS_V - Ro_\tau U = \frac{\partial P}{\partial y}, \quad (5)$$

$$-\left(-\frac{4U}{U_b} + V\frac{\partial\Theta}{\partial y} + W\frac{\partial\Theta}{\partial z}\right) + \frac{1}{Pr\ Re_\tau}\left(\frac{\partial^2\Theta}{\partial y^2} + \frac{\partial^2\Theta}{\partial z^2}\right) - \left(\frac{\partial\langle v'\theta'\rangle}{\partial y} + \frac{\partial\langle w'\theta'\rangle}{\partial z}\right) + SGS_\Theta = 0. \quad (6)$$

The different terms of Eqs. (4)–(6) are responsible, from left to right, for the convective, diffusion, and turbulent transport. The fourth terms in Eqs. (4)–(6) correspond to the SGS transport and the fifth terms in Eqs. (4) and (5) are the x and y components of the Coriolis acceleration. The terms on the right side of Eqs. (4) and (5) represent the average pressure gradient along the x- and y-directions, respectively.

Figures 4–6 show the different terms of the momentum and thermal energy budgets, as they appear in Eqs. (4)–(6), along the wall bisectors $z=0.5$ [Figs. 4(a) and 6(a)] and $y=0.5$ [Figs. 4(b), 5, and 6(b)] at the highest rotation rate analyzed in this study ($Ro_\tau=40$). The averaged profiles of velocity and temperature are also included in these figures. At $Ro_\tau=40$ the SGS terms make no significant contribution to the momentum and thermal energy budgets and have been omitted in Figs. 4–6.

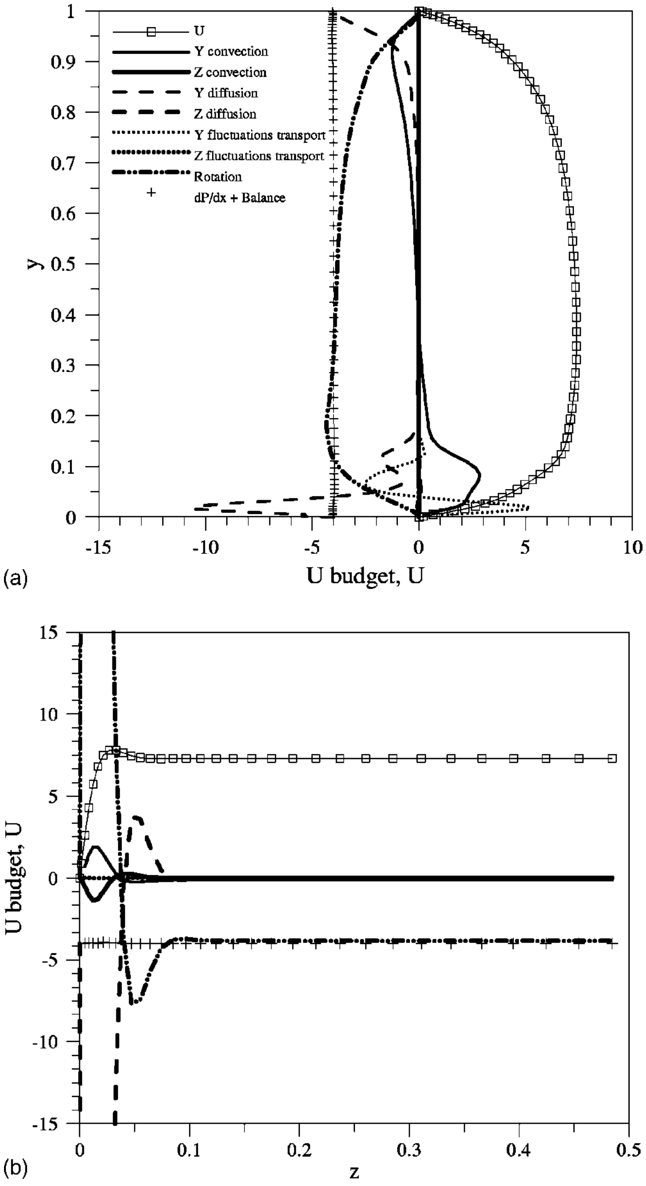

FIG. 4. Time averaged x-momentum budget at $\mathrm{Ro}_\tau=40$ along the lines (a) $z=0.5$ and (b) $y=0.5$.

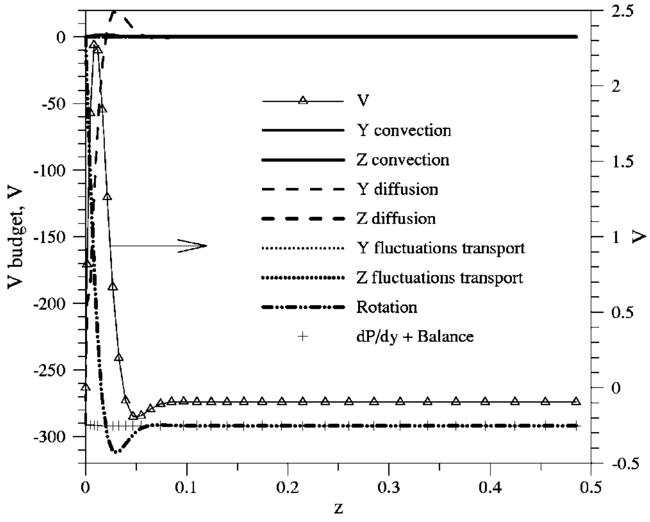

FIG. 5. Time averaged y-momentum budget at $\mathrm{Ro}_\tau=40$ along the line $y=0.5$.

Figure 4(a) shows that the x-momentum near the stable wall ($y=1$) is generated by the mean pressure gradient. This term is balanced, close to the wall, by the viscous diffusion and, in the central part of the duct, by the Coriolis term ($\mathrm{Ro}_\tau V$), which is responsible for the reduction of the streamwise velocity component as the rotation rate is increased. Near the unstable wall ($y=0$) the important contributions of the fluctuation transport terms to the x-momentum and thermal energy shown in Figs. 4(a) and 6(a) indicate that the flow in this region is unsteady even at this low Reynolds number ($\mathrm{Re}=1810$).

As shown in Fig. 2, at high rotation rates ($\mathrm{Ro}_\tau \geqslant 20$) the secondary flow, which consists in two large stretched cells, generates thin boundary layers near the sidewalls. These boundary layers are the major contributors to the overall head loss of the flow as can be inferred from the concentration of the contour levels near the sidewalls in Fig. 2. Figures 4(b) and 5 show the x- and y-momentum budgets across these boundary layers. It can be seen in Fig. 4(b) that near the sidewall $z=0$ the imposed pressure gradient along the x-direction is balanced mainly by the viscous diffusion along the z direction and the Coriolis term. The different contributions of the terms of the x-momentum budget shown in Fig. 4(b) allow rewriting Eq. (4) near the sidewalls as

$$\frac{1}{\mathrm{Re}_\tau}\left(\frac{\partial^2 U}{\partial z^2}\right)+\mathrm{Ro}_\tau V \approx -4 \tag{7}$$

and in the central part of the duct as

$$\mathrm{Ro}_\tau V_c \approx -4. \tag{8}$$

At high rotation rates the vertical velocity component is approximately constant in the central part of the duct [see Figs. 2(f) and 5] and its value is denoted in Eq. (8) as $V_c, V_c \approx -4/\mathrm{Ro}_\tau$.

Similarly, the simplified y-momentum budget shown in Fig. 5 near the sidewalls and in the central part of the duct are

$$\frac{1}{\mathrm{Re}_\tau}\left(\frac{\partial^2 V}{\partial z^2}\right)-\mathrm{Ro}_\tau U \approx \frac{\partial P}{\partial y} \tag{9}$$

and

$$-\mathrm{Ro}_\tau U_c \approx \frac{\partial P}{\partial y}, \tag{10}$$

respectively. Figure 5 shows that pressure does not depend on z ($\partial P/\partial y$ is constant along the z direction) indicating that the W velocity component is negligibly small compared with V [see, for example, Fig. 2(f)]. Inspection of the momentum budgets at high rotation rates and at different y positions shows that Eqs. (7)–(10) are valid approximations of the complete momentum budgets in most of the cross section of the duct, as can be inferred from the flow topology in Fig. 2(f).

Rearranging Eqs. (9) and (10), the simplified y-momentum budget can be written as

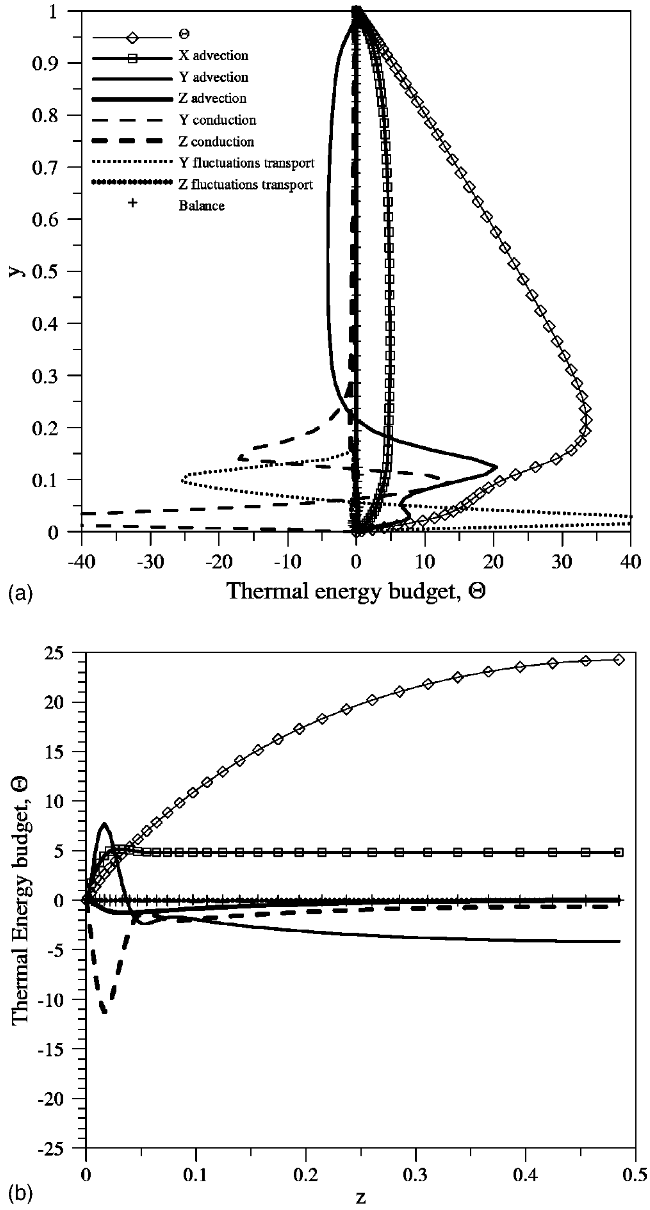

FIG. 6. Time averaged thermal energy budget at $\mathrm{Ro}_\tau=40$ along the lines (a) $z=0.5$ and (b) $y=0.5$.

$$\frac{1}{\mathrm{Re}_\tau}\left(\frac{\partial^2 V}{\partial z^2}\right) - \mathrm{Ro}_\tau (U - U_c) \approx 0. \tag{11}$$

The boundary conditions for Eqs. (7) and (11) are at $z=0, U=0, V=0$ and at $(z/\sqrt{\mathrm{Ek}})\rightarrow\infty, U=U_c, V=V_c$. The solutions to Eqs. (7) and (11) and the corresponding boundary conditions can be expressed as

$$U = U_c\left(1 - \cos\left(\frac{z}{\sqrt{\mathrm{Ek}}}\right)e^{-z/\sqrt{\mathrm{Ek}}}\right) - V_c\left(\sin\left(\frac{z}{\sqrt{\mathrm{Ek}}}\right)e^{-z/\sqrt{\mathrm{Ek}}}\right), \tag{12}$$

$$V = V_c\left(1 - \cos\left(\frac{z}{\sqrt{\mathrm{Ek}}}\right)e^{-z/\sqrt{\mathrm{Ek}}}\right) + U_c\left(\sin\left(\frac{z}{\sqrt{\mathrm{Ek}}}\right)e^{-z/\sqrt{\mathrm{Ek}}}\right), \tag{13}$$

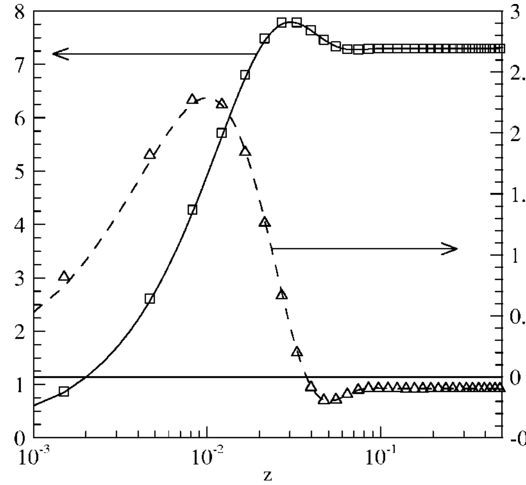

FIG. 7. Profiles of the streamwise and the y-velocity component at $\mathrm{Ro}_\tau=40$ along the line $y=0.5$. Lines: model given by Eqs. (12) and (13). Symbols: numerical simulation.

where Ek is the Ekman number ($\mathrm{Ek}=\nu/\Omega\mathrm{D}^2=2/\mathrm{RoRe}$). The only unknown parameter in Eqs. (12) and (13) is the streamwise velocity component in the center of the duct, U_c, since $V_c=-4/\mathrm{Ro}_\tau$ according to Eq. (8). The values of the derivatives of the profiles of Eqs. (12) and (13) at the symmetry midplane $z=0.5$ are proportional to $e^{-1/2\sqrt{\mathrm{Ek}}}$ and consequently negligibly small at high rotation rates (i.e., small values of Ek). It can be seen in Fig. 7 that the numerically predicted velocity profiles at $\mathrm{Ro}_\tau=40$ along the line $y=0.5$ agree with the analytical solutions using the value of U_c obtained in the simulations. A similar agreement between the analytical solutions and the numerical results is found in the range $0.15<y<0.85$ at $\mathrm{Ro}_\tau=40$. An estimation of U_c can be obtained by imposing that the averaged vertical velocity profile given in Eq. (13) in the range $0\leqslant z\leqslant 0.5$ is zero (i.e., the descending flow rate pumped by the Coriolis force in the central part of the duct is equal to ascending the flow rate within the vertical boundary layer):

$$U_c \approx V_c(1 - 1/\sqrt{\mathrm{Ek}}). \tag{14}$$

The use of Eqs. (12) and (13) to predict the velocity profiles is subjected to the validity of the simplified momentum budgets of Eqs. (7), (8), and (11). These equations express the balance between the pressure gradient terms, the Coriolis acceleration and the viscous term within the Ekman layer. In the central part of the duct where the flow has been relaminarized by the effect of rotation the balance is produced by the pressure gradient terms and the Coriolis terms. At moderate rotation rates ($1.5\leqslant\mathrm{Ro}_\tau\leqslant 10$) the vertical convection of x-momentum $(-V\partial U/\partial y)$ contributes, in the central part of the duct, together with the Coriolis term $(\mathrm{Ro}_\tau V)$ to balance the imposed pressure gradient along the x-direction. For example, the ratio $(-V\partial U/\partial y)/(\mathrm{Ro}_\tau V)$ in the central part of the duct is about 12 at $\mathrm{Ro}_\tau=1.5$, 0.9 at $\mathrm{Ro}_\tau=10$, 0.2 at $\mathrm{Ro}_\tau=20$ and 0.03 at $\mathrm{Ro}_\tau=40$. Consequently, the velocity profiles of Eqs. (12) and (13) can be used to estimate boundary layer quantities for $\mathrm{Ro}_\tau\geqslant 20$. For example, the boundary layer thicknesses defined as the distance from the wall to the position of the maximum velocity are for $U, \delta_U\approx 3\pi\mathrm{Ek}^{1/2}/4$ and for $V, \delta_V\approx \pi\mathrm{Ek}^{1/2}/4$.

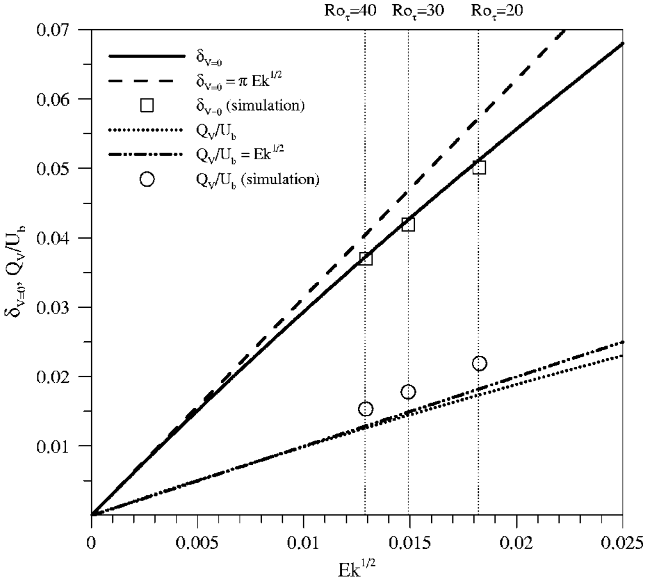

FIG. 8. Evolution of $\delta_{V=0}$ and the ratio between the secondary and the streamwise flow rates (Q_V/U_b) as a function of $\mathrm{Ek}^{1/2}$.

The non-dimensional bulk velocity $(U_b=\overline{U_b}/u_\tau)$ can be computed integrating Eq. (12) as

$$U_b \approx 2\int_0^{1/2} U dz \approx U_c \frac{(1-\sqrt{\mathrm{Ek}})^2+\sqrt{\mathrm{Ek}}}{1-\sqrt{\mathrm{Ek}}} + O(e^{-1/2\sqrt{\mathrm{Ek}}}). \tag{15}$$

The last term in Eq. (15) represents a set of terms that are proportional to $e^{-1/2\sqrt{\mathrm{Ek}}}$ and consequently can be neglected at high rotation rates. Equation (15) assumes that the velocity profiles along the z direction, given in Eqs. (12) and (13), are valid for most of the cross section of the duct [i.e., U_c and V_c in Eq. (15) are considered constant along the y direction].

The ratio between the non-dimensional secondary flow rate per unit length (Q_V) pumped by the Coriolis force and the non-dimensional bulk velocity (or the streamwise flow rate) is

$$\frac{Q_V}{U_b} = \frac{2}{U_b}\int_{z=0}^{\delta_{V=0}} V dz \tag{16}$$

where $\delta_V=0$ is the non-dimensional distance from the sidewall to the position where $V=0$ (see Figs. 5 and 7). This distance can be computed using the vertical velocity profile of Eq. (13). Figure 8 shows that $\delta_V=0$ decreases monotonically, as the Ekman/rotation number is decreased/increased and that the simulations at $\mathrm{Ro}_\tau \geqslant 20$ reproduce accurately the theoretical results. As shown in Fig. 8 an approximate expression for $\delta_{V=0}$ $(\delta_{V=0}=\pi \mathrm{Ek}^{1/2})$ can be used for $\mathrm{Ek}<0.01$ with a 6% of error. The ratio expressed in Eq. (16) is also plotted in Fig. 8 using the exact dependence of $\delta_{V=0}$ on the Ekman number included in this figure. Equation (15) has been used to calculate U_b in Eq. (16). It can be seen that the square root of the Ekman layer characterizes the ratio between the secondary and the streamwise flow rate for $\mathrm{Ek} < 0.02$. The values of this ratio computed with the results of the numerical simulation are shown in Fig. 8 and are about 10–20% larger because of the difference between the values of U_b obtained using Eq. (15) and those of the simulations.

Figures 2(f) and 6(a) show that, along the line $z=0.5$, the thermal energy from the stable wall $(y=1)$ is advected along the x and y directions by the streamwise velocity component and by the Coriolis generated vertical velocity component. According to this the thermal energy equation [Eq. (6)] in this region can be written as

$$\frac{4U}{U_b} - V\frac{\partial\Theta}{\partial y} \approx 0. \tag{17}$$

The temperature gradient, which is moderately constant in the stable region of the flow along the vertical symmetry plane of the duct as shown in Fig. 6(a), can be estimated using Eq. (17) and considering that $U_c/U_b \approx 1$ and $V=V_c \approx -4/\mathrm{Ro}_\tau$,

$$\frac{\partial\Theta}{\partial y} \approx \frac{4U_c}{U_b V_c} \approx -\mathrm{Ro}_\tau. \tag{18}$$

Figure 6(b) shows that near the vertical walls, where the Ekman layers develop, the main contributors to the thermal energy budget are the x- and y-advection terms and the heat conduction term along the z direction. According to this the simplified energy equation is

$$-\left(-\frac{4U}{U_b} + V\frac{\partial\Theta}{\partial y}\right) + \frac{1}{\mathrm{Pr\,Re}_\tau}\left(\frac{\partial^2\Theta}{\partial z^2}\right) = 0. \tag{19}$$

The important contribution of the y-advection term $(V\partial\Theta/\partial y)$ at high rotation rates shown in Fig. 6(b) is responsible for the dependence of temperature on y and z [see, for example, Figs. 2(d)–2(f)] and prevents the closed solution of Eq. (19) using the velocity profiles of Eqs. (12) and (13).

C. Friction coefficients and Nusselt numbers

Figures 9(a) and 9(b) show the numerically predicted overall friction coefficient $(\mathrm{Cf}=2\tau_w/\rho\overline{U_b^2})$ and Nusselt number $(\mathrm{Nu}=hD/k)$ as a function of $\mathrm{Ek}^{1/2}$. The data for the isothermal rotating duct flow reported by Pallares and Davidson[5] in the range $\mathrm{Ro}_\tau \leqslant 1.5$ are also plotted in Fig. 9(a). The averaged friction coefficients and Nusselt numbers at the unstable $(y=0,\ \mathrm{Cf}_u$ and $\mathrm{Nu}_u)$, stable $(y=1,\ \mathrm{Cf}_s$ and $\mathrm{Nu}_s)$ and at the two lateral walls $(z=0$ and $z=1,\ \mathrm{Cf}_\mathrm{l}$ and $\mathrm{Nu}_\mathrm{l})$ are also plotted in Figs. 9(a) and 9(b). Note that by definition, $\mathrm{Cf}=\mathrm{Cf}_u+\mathrm{Cf}_s+\mathrm{Cf}_\mathrm{l}$ and $\mathrm{Nu}=\mathrm{Nu}_u+\mathrm{Nu}_s+\mathrm{Nu}_\mathrm{l}$. The overall friction coefficient and Nusselt numbers for non-rotating square duct flow $(\mathrm{Cf}_\mathrm{nr}$ and $\mathrm{Nu}_\mathrm{nr})$ at the corresponding Reynolds number predicted by the closed solution of the flow and energy equations in the laminar regime[11] and by the conventional correlations in the turbulent regime[12,13] have also been included in Fig. 9 for comparison. The local friction coefficient and $(\mathrm{Cf}_\mathrm{nr}/4=\mathrm{Cf}_u=\mathrm{Cf}_s=\mathrm{Cf}_\mathrm{l}/2$ and $\mathrm{Nu}_\mathrm{nr}/4=\mathrm{Nu}_u=\mathrm{Nu}_s=\mathrm{Nu}_\mathrm{l}/2)$ are also indicated in this figure.

Figure 9(a) shows that the local friction coefficients on the unstable wall and on the lateral walls are larger in comparison with the non-rotating case. It can be seen that the local friction coefficient corresponding to the sidewalls is the main contributor to the total head loss at high rotation rates.

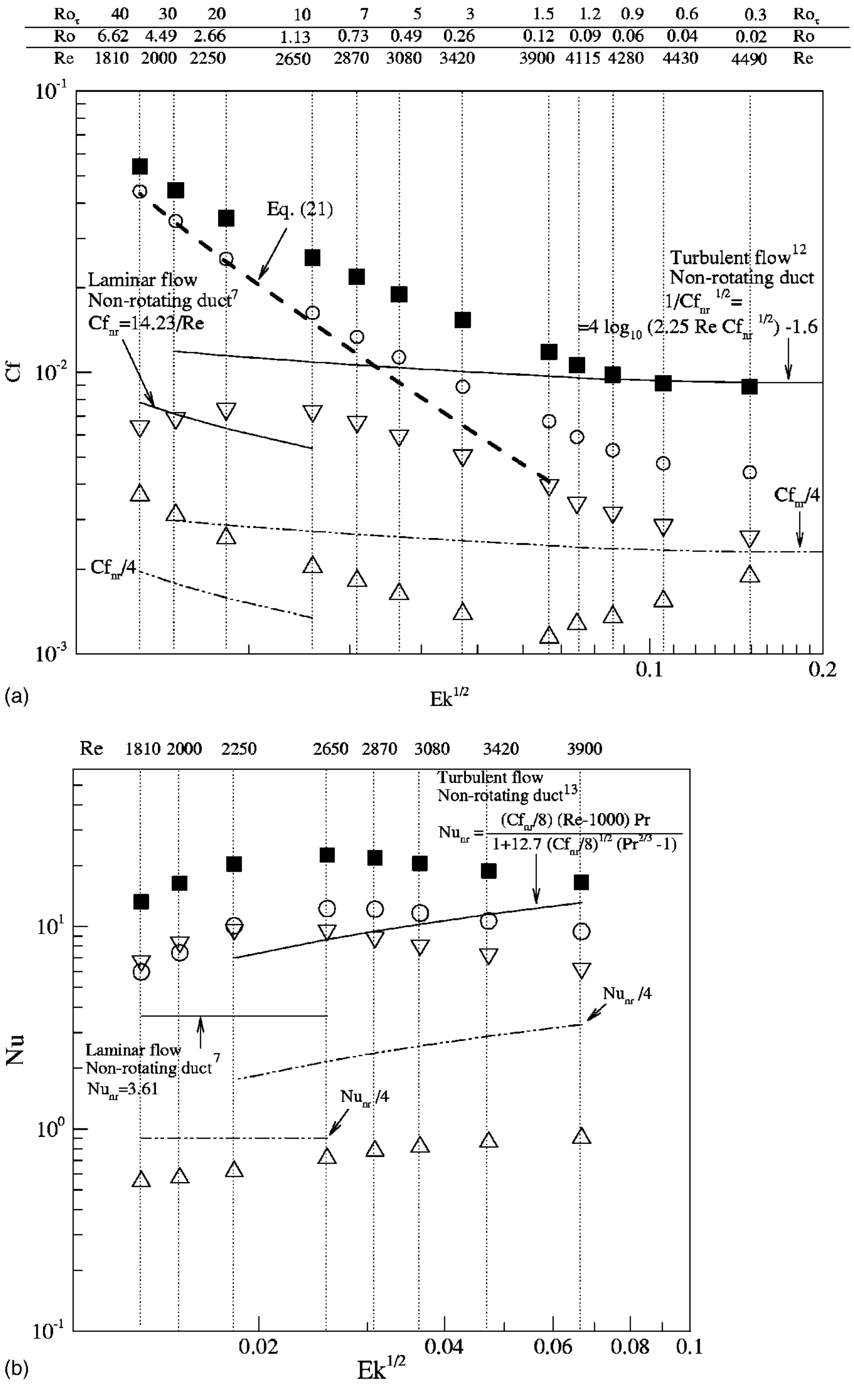

FIG. 9. (a) Overall and wall averaged friction coefficients and (b) Nusselt numbers. Filled symbols: overall quantities. Open symbols: wall averaged quantity along (○) the sidewalls $z=0$ and $z=1$, (▽) the unstable wall, $y=0$, and (△) the stable wall, $y=1$. The Reynolds and rotation numbers based on the bulk velocity corresponding to the different Ekman numbers are indicated at the top of the figure. The friction coefficients predicted by Pallares and Davidson (Ref. 5) in the range $\mathrm{Ro}_\tau \leqslant 1.5$ $(\mathrm{Re} \geqslant 3900)$ are also included in this figure.

At $\mathrm{Ro}_\tau=40$, the average wall shear stress associated with the boundary layers near the two lateral walls is responsible for 80% of the total head loss. The local friction coefficient on the unstable wall is the second most important contributor to the overall head loss of the flow. At $\mathrm{Ro}_\tau=1.5$ its contribution is about 33% and only 12% at $\mathrm{Ro}_\tau=40$. Note that the contribution of each individual wall is 25% for the non-rotating case. The contribution of the friction coefficient on the stable wall, about 10% at $\mathrm{Ro}_\tau=1.5$ and 7% at $\mathrm{Ro}_\tau=40$, is less sensitive to the rotation rate in the range $\mathrm{Ro}_\tau>1.5$ which corresponds to the complete suppression of the turbulence near this wall.

The values of the friction coefficient on the lateral walls at high rotation rates can be predicted using the solution of the simplified momentum budgets analyzed above. The ratio U_b/U_c of Eq. (15) and the dependence of U_c on V_c of Eq. (14) can be used to express the ratio U_b/V_c as

$$\frac{U_b}{V_c} = 1 - \left(\frac{1}{\sqrt{\mathrm{Ek}}} + \sqrt{\mathrm{Ek}}\right). \tag{20}$$

Considering that $V_c \approx -4/\mathrm{Ro}_\tau$, Eq. (20) can be rewritten as

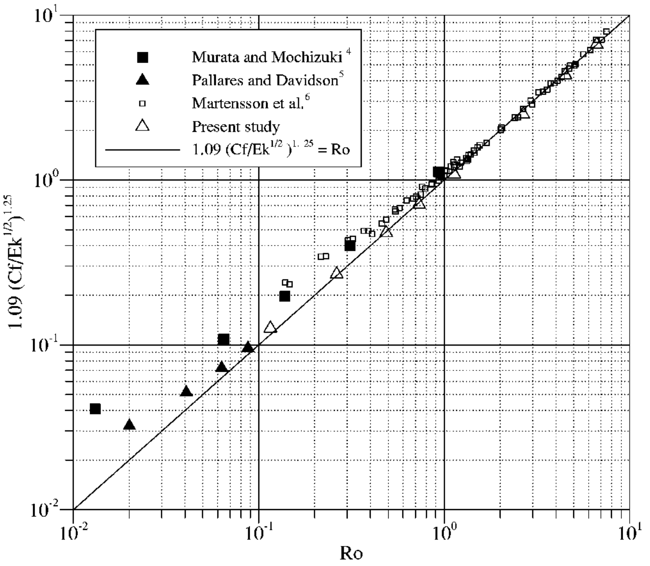

FIG. 10. Overall friction coefficient in a rotating square duct.

$$\mathrm{Cf}_l = \frac{\mathrm{Ro}\sqrt{\mathrm{Ek}}}{2}\frac{1}{1-\sqrt{\mathrm{Ek}}+\mathrm{Ek}}, \qquad (21)$$

where Cf_l is the friction coefficient at the two sidewalls. Figure 9(a) shows that Eq. (21) reproduces accurately the Cf_l in the range $\mathrm{Ro}_\tau \geqslant 20$ according to the fact that in this range of rotational numbers a balance between the Coriolis force and the imposed pressure gradient is established in most of the area of the cross section of the duct.

Figure 9(b) shows that, as the rotation number is increased in the range $\mathrm{Ro}_\tau \leqslant 10$, the local Nusselt numbers on the unstable and on the lateral walls are monotonically increased, in comparison with the non-rotating case, while the heat transfer rates are reduced on the stable wall. As shown in Fig. 3 there is an important reduction of the fluctuation intensities and, thus, of the turbulent transport terms at $\mathrm{Ro}_\tau > 1.5$. Consequently the progressive increase, as the rotation rate is increased, of the heat transfer rates, in comparison with the non-rotating case, can be attributed to the enhancement of the advective transport established by the Coriolis generated secondary flows. The local Nusselt number on the unstable wall is the main contribution to the overall Nusselt number in the range of rotational numbers considered with contributions ranging from 37% at $\mathrm{Ro}_\tau = 1.5$ to 51% at $\mathrm{Ro}_\tau = 40$. The local Nusselt number on the stable wall only is responsible for the 4–5% of the overall heat transfer rate.

Figure 10 shows the overall friction coefficient for rotating square duct flow. This figure includes the data from the LES reported in Murata and Mochizuki[4] ($7530 \leqslant \mathrm{Re} \leqslant 10\,660, 0.013 \leqslant \mathrm{Ro} \leqslant 0.930$) and Pallares and Davidson[5] ($4120 \leqslant \mathrm{Re} \leqslant 4500, 0.010 \leqslant \mathrm{Ro} \leqslant 0.087$), the experiments by Mårtensson *et al.*[6] ($10^4 \leqslant \mathrm{Re} \leqslant 2 \times 10^4, 0.15 \leqslant \mathrm{Ro} \leqslant 7.5$) and the results of the present work ($1810 \leqslant \mathrm{Re} \leqslant 3420, 0.12 \leqslant \mathrm{Ro} \leqslant 6.62$). It can be seen that the data plotted in Fig. 10 in the range $\mathrm{Ro} \geqslant 1$ are well correlated with Eq. (22) that relates the friction coefficient, the rotation and the Ekman numbers similarly to Eq. (21):

$$1.09(\mathrm{Cf}/\sqrt{\mathrm{Ek}})^{1.25} = \mathrm{Ro}. \qquad (22)$$

The differences between the overall friction coefficient predicted by Eq. (22) and the data plotted in Fig. 10 at $\mathrm{Ro} \geqslant 1$ are within 5% of even the large difference of Reynolds numbers between the measurements of Mårtensson *et al.*,[6] $O(\mathrm{Re}) = 10^4$, and the present numerical simulations, $O(\mathrm{Re}) = 10^3$. Figure 10 shows that at $\mathrm{Ro} < 1$ the agreement between Eq. (22) and the numerical and experimental data depends on the Reynolds number. In fact Eq. (22) reproduces accurately the predictions at low Reynolds numbers of the present study while underpredicts by 50–10 % at $\mathrm{Ro} < 1$ the experimental data measured at larger Reynolds numbers ($\mathrm{Re} \approx 10^4$). This indicates that the validity of Eq. (22) can be extended to $\mathrm{Ro} < 1$ at low Reynolds numbers.

IV. CONCLUSIONS

This study analyzes numerical simulations of fully developed forced convection of air ($\mathrm{Pr} = 0.7$) in a square duct rotating at high rotation rates. Special attention is given to the effects of rotation on the local and overall heat transfer rates and wall shear stresses. The non-dimensional numbers that characterize these quantities, the Nusselt number and the friction coefficient depend strongly on the Reynolds and rotation number. As the rotation rate is increased there is a progressive reduction of the fluctuation intensities of the velocity components. The suppression of the fluctuation intensities is initiated near the wall where the stratification of the streamwise momentum component is stable with respect to the Coriolis force. On this wall there is a considerable reduction of the wall shear stress and the heat transfer coefficients in comparison with the non-rotating case. The secondary flows produced by the Coriolis acceleration convect low momentum fluid from the stable wall to the unstable wall and progressively reduces the extension of the flow where the stratification of the x-momentum is unstable with respect the Coriolis force, as the rotation rate is increased. At low Reynolds numbers ($\mathrm{Re} \approx 2000$) the unstable stratification maintains the unsteadiness of the flow in this region and the local Nusselt numbers and friction coefficient on the unstable wall are larger in comparison with the non-rotation case. On the other two walls of the duct that are perpendicular to the rotation axis the secondary flows generates Ekman layers that are responsible for most of the pressure drop of the flow. At high rotation rates the boundary layer quantities can be predicted accurately with the closed solution of the corresponding simplified momentum budgets. The alterations that rotation induces in the flow such as the persistent secondary flows and the subsistence of an unsteady flow near the unstable wall produce overall friction coefficients and Nusselt numbers larger than the non-rotation case.

ACKNOWLEDGMENTS

Part of this work was carried out during the first author's visit at Chalmers. This study was financially supported by the Department of Thermo and Fluid Dynamics (Chalmers University of Technology) and by the Spanish Ministry of Science of Technology under projects DPI2000-1578-C02-

01, DPI2003-06725-C02-01 and VEM2003-20048. We would like to thank A. Murata and G. E. Mårtensson for providing us original data of their works.

[1] J. P. Johnston, R. M. Hallen, and D. K. Lezius, "Effects of spanwise rotation on the structure of two-dimensional fully developed turbulent channel flow," J. Fluid Mech. **56**, 533 (1972).

[2] R. Kristoffersen and H. Andersson, "Direct simulations of low-Reynolds-number turbulent flow in a rotating channel," J. Fluid Mech. **256**, 163 (1993).

[3] K. Alvelius, "Studies of turbulence and its modelling through large eddy- and direct numerical simulation," Ph.D. thesis, Department of Mechanics, Royal Institute of Technology, Stockolm, 1999.

[4] A. Murata and S. Mochizuki, "Effect of cross-sectional aspect ratio on turbulent heat transfer in an orthogonally rotating rectangular smooth duct," Int. J. Heat Mass Transfer **42**, 3803 (1999).

[5] J. Pallares and L. Davidson, "Large-eddy simulations of turbulent flow in a rotating square duct," Phys. Fluids **12**, 2878 (2000).

[6] G. E. Mårtensson, J. Gunnarsson, A. V. Johansson, and H. Moberg, "Experimental investigation of a rapidly rotating turbulent duct flow," Exp. Fluids **33**, 482 (2002).

[7] R. K. Shah and A. L. London "Laminar flow forced convection in ducts," in *Advances in Heat Transfer* (Academic, New York, 1978).

[8] W. Kim and S. Menon, "Application of the localized dynamic subgrid-scale model to turbulent wall-bounded flows," AIAA Paper 97-0210, 35th Aerospace Sciences Meeting & Exhibit, Reno, NV, 1997.

[9] A. Sohankar, L. Davidson, and C. Norberg, "Large eddy simulation of flow past a square cylinder: Comparison of different subgrid scale models," J. Fluids Eng. **122**, 39 (2000); see also **122**, 643 (2000).

[10] J. Pallares and L. Davidson "Large-eddy simulations of turbulent heat transfer in stationary and rotating square ducts," Phys. Fluids **14**, 2804 (2002).

[11] J. Pallares and L. Davidson, "Large-eddy simulation of turbulent flows in stationary and rotating channels and in a stationary duct," Report No. 00/03, Department of Thermo and Fluid Dynamics, Chalmers University of Technology, Gothenburg, Sweden, 2000.

[12] O. C. Jones, "An improvement in the calculation of turbulent friction in rectangular ducts," J. Fluids Eng. **98**, 173 (1976).

[13] V. Gnieliski, "New equations for heat and mass transfer in turbulent pipe and channel flow," Int. Chem. Eng. **16**, 359 (1976).